The Status of MUSIC: The Multiwavelength Sub/millimeter Inductance Camera

Jack Sayers[a], Clint Bockstiegel[b], Spencer Brugger[c], Nicole G. Czakon[d], Peter K. Day[e], Thomas P. Downes[f], Ran P. Duan[a], Jiansong Gao[b], Amandeep K. Gill[c], Jason Glenn[c], Sunil R. Golwala[a], Matt I. Hollister[a], Albert Lam[a], Henry G. LeDuc[e], Philip R. Maloney[c], Benjamin A. Mazin[g], Sean G. McHugh[g], David A. Miller[a], Anthony K. Mroczkowski[h], Omid Noroozian[i], Hien T. Nguyen[e], James A. Schlaerth[a], Seth R. Siegel[a], Anastasios Vayonakis[a], Philip R. Wilson[e], and Jonas Zmuidzinas[a,e]

[a]California Institute of Technology, Pasadena, CA 91125 USA;
[b]National Institute of Standards and Technology, Boulder, CO 80305 USA;
[c]University of Colorado, Boulder, CO 80309 USA;
[d]Academia Sinica, Taipei 10617 Taiwan;
[e]Jet Propulsion Lab, Pasadena, CA 91109 USA;
[f]University of Wisconsin, Milwaukee, WI 53201 USA;
[g]University of California, Santa Barbara, CA 93106 USA;
[h]US Naval Research Laboratory, Washington, DC 20375 USA;
[i]Goddard Space Flight Center, Greenbelt, MD 20771 USA

ABSTRACT

The Multiwavelength Sub/millimeter Inductance Camera (MUSIC) is a four-band photometric imaging camera operating from the Caltech Submillimeter Observatory (CSO). MUSIC is designed to utilize 2304 microwave kinetic inductance detectors (MKIDs), with 576 MKIDs for each observing band centered on 150, 230, 290, and 350 GHz. MUSIC's field of view (FOV) is $14'$ square, and the point-spread functions (PSFs) in the four observing bands have $45''$, $31''$, $25''$, and $22''$ full-widths at half maximum (FWHM). The camera was installed in April 2012 with 25% of its nominal detector count in each band, and has subsequently completed three short sets of engineering observations and one longer duration set of early science observations. Recent results from on-sky characterization of the instrument during these observing runs are presented, including achieved map-based sensitivities from deep integrations, along with results from lab-based measurements made during the same period. In addition, recent upgrades to MUSIC, which are expected to significantly improve the sensitivity of the camera, are described.

Keywords: kinetic inductance detectors, millimeter-wave instrumentation, submillimeter instrumentation, low-temperature detectors

1. SCIENTIFIC MOTIVATION

MUSIC has been designed to simultaneously produce sub/millimeter images in four photometric observing bands with $\simeq 30''$ resolution. With a $14'$ FOV, MUSIC can deliver relatively small images for detailed studies of single objects or regions ($\simeq 0.1$ deg^2), along with survey-sized maps of up to 10s of deg^2. Given these capabilities, MUSIC is ideally suited for the study of dusty star-forming galaxies, cold cores within our own galaxy, and the gaseous intracluster medium (ICM) of massive galaxy clusters via the Sunyaev-Zel'dovich (SZ) effect. A brief overview of some of the science that can be derived from observations of these objects is given below.

Approximately half of the energy radiated by stellar nucleosynthesis over the history of the universe is absorbed by dust and re-radiated at infrared and submillimeter wavelengths.[1,2] Recent measurements, mainly

Further author information: (Send correspondence to Jack Sayers)
E-mail: jack@caltech.edu.edu, Telephone: 1 626 395 2892

Millimeter, Submillimeter, and Far-Infrared Detectors and Instrumentation for Astronomy VII, edited by Wayne S. Holland, Jonas Zmuidzinas, Proc. of SPIE Vol. 9153, 915304 · © 2014 SPIE · CCC code: 0277-786X/14/$18 · doi: 10.1117/12.2055444

at far infrared and short submillimeter wavelengths, indicate that this cosmic infrared background (CIB) can be resolved into individual galaxies, many of which reside in the redshift range $1 \lesssim z \lesssim 4$ and trace the peak in cosmic star formation (e.g., Refs. 3, 4). Lower frequency observations, such as those that MUSIC will provide, preferentially select higher redshift galaxies and can extend these studies to the more distant universe (e.g., Ref. 5). In addition, the spectral coverage provided by MUSIC can be combined with higher frequency data to obtain more robust estimates of the total luminosities, star formation rates, and dust properties of these galaxies, along with more reliable selections of interesting high-z objects for further study from other facilities (e.g., Ref. 5).

On smaller physical scales, observations of prestellar cores and young stellar objects within our own galaxy can provide details of the early stages of star formation (e.g., Ref 6). In particular, the MUSIC observing bands will allow for detections of even the coldest cores, and the multiple long wavelength bands provide for robust mass estimates.

Galaxy clusters are the largest bound objects in the universe, and they therefore provide an ideal window to study the physical processes involved in structure formation. MUSIC aims to probe the ICM of these objects via the kinetic and thermal SZ effects in order to provide information on, for example, the velocity structure, thermal pressure, and entropy of the ICM, particularly near the cluster virial radius where active accretion is ongoing (e.g., Ref. 7). Such observations are an ideal complement to existing and upcoming X-ray data, which provide detailed measurements of the ICM properties in the inner regions of the cluster but in general cannot be extended to the virial radius (e.g., Refs. 8–10).

The recently completed satellite missions *Herschel* and *Planck* have provided a wealth of sub/millimeter observations of dusty star-forming galaxies, cold cores within our galaxy, and galaxy clusters (e.g., Refs. 11–13). However, *Herschel* lacks spectral coverage below 600 GHz, which in general falls near or above the peak in the spectral energy distributions of both dusty star-forming galaxies and cold cores, therefore preventing robust determinations of the full spectral energy distributions of these objects. In addition, the *Herschel* bands are well suited to measure relativistic corrections to the SZ spectrum, but such measurements can only be made with the addition of low frequency observations where the relativistic corrections are minimal. In contrast, *Planck* provides excellent spectral coverage across the sub/millimeter band, but it has extremely coarse angular resolution with FWHMs $\geq 5'$. As a result, it is generally not possible to identify single galaxies or cores in the *Planck* data (and there are often multiple sources within a single *Planck* detection). In addition, *Planck* is also not able to resolve the SZ signal from most clusters. MUSIC is therefore an ideal complement to the exquisite data delivered by these two satellites. It provides the long-wavelength coverage required to fully characterize many of of the *Herschel*-detected objects, and it provides the angular resolution required to isolate the individual source(s) that comprise the *Planck* detections.

2. MUSIC INSTRUMENT

MUSIC was installed at the CSO in May 2012, and has been in operation since that time. The MUSIC instrument has been described in detail by Refs. 14–20, and therefore a very general overview is provided below, focusing on the major design and performance aspects along with recent improvements to the instrument.

2.1 Focal Plane

MUSIC has been designed around a focal plane populated with 2304 optically coupled MKIDs (see Figure 1). The MKIDs are superconducting resonators; optical power absorbed in the detector breaks cooper pairs, leading to a change in surface impedance which in turn results in a shift in the quality factor and resonant frequency of the MKID.[21] For MUSIC, each MKID resonator consists of an interdigitated capacitor (IDC) and a coplanar waveguide (CPW) inductive section. The MKIDs are entirely niobium, with the exception of a short aluminum section at the end of the CPW which is used to absorb the optical power. To sense changes in the resonances, a niobium CPW feedline is coupled to the IDC portion of each resonator.

The MUSIC focal plane consists of eight separate tiles, each with one feedline coupled to 288 MKIDs. Within each tile, the geometry of the IDC is adjusted to give each MKID a unique resonance frequency between 3–4 GHz in order to facilitate readout using a single feedline. Optical power is coupled to the aluminum section of the

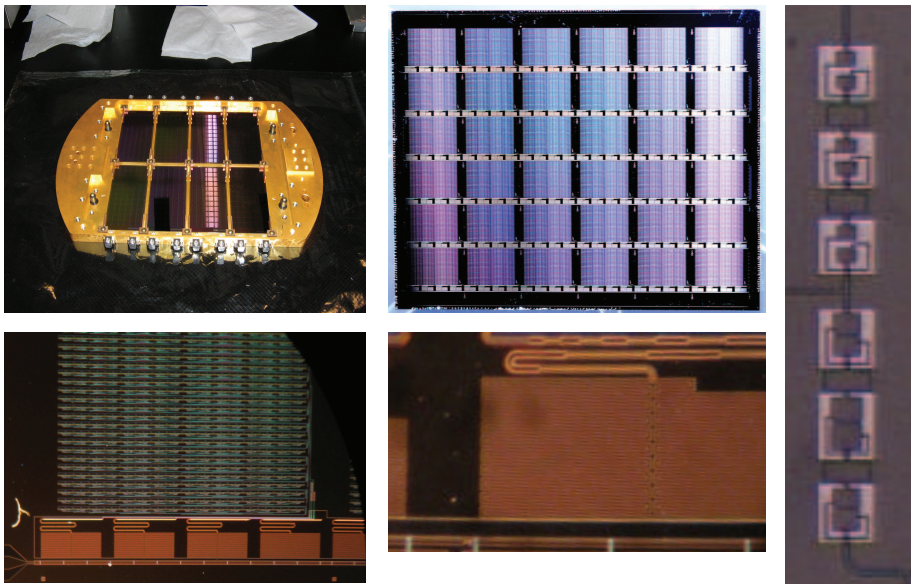

Figure 1. The MUSIC focal plane. Clockwise from upper left: The eight-tile focal plane with 2304 MKIDs; half of a single tile, showing 36 antennas and 144 MKIDs; two sets of lumped-element bandpass filters (this is an engineering-grade two-band device, the science-grade devices have four sets of filters); a single MKID with the IDC at the bottom and the inductive CPW with stepped-impedance filters at the top; a single antenna at the top with four MKIDs across the bottom (three sets of lumped-element filters can be seen at the bottom right of the antenna – one of the four MKIDs is not optically coupled in this case).

MKID via a niobium microstrip connected to a slot-dipole phased-array antenna, which is also niobium.[22,23] By design, the antenna is efficient over a large bandwidth of approximately two octaves, and three-pole Butterworth lumped-element bandpass filters are placed along the microstrip to define the desired observing bands.[24] A single focal plane tile consists of 72 antennas, and the microstrip from each antenna branches in order to couple to four separate MKIDs with non-overlapping observing bands centered at approximately 150, 230, 290, and 350 GHz.

As described in detail in Ref. 19, the exact geometry of the resonators was chosen primarily based on noise performance and stray-light susceptibility. In particular, IDCs were used for the capacitive portion of the MKID in order to minimize the two-level system (TLS) noise.[25] The TLS noise decreases with increasing IDC size, thus motivating large IDCs. However, enlarging the IDC increases its fractional footprint on the focal plane at the expense of the antenna, and consequently reduces the overall optical efficiency of the camera. For MUSIC, an IDC producing an MKID footprint of 0.7 mm^2 was chosen, which results in a 71% fill fraction for the antennas. The measured TLS noise is in good agreement with expectations, as described in detail in Ref. 20. However, because the IDC size decreases with increasing resonance frequency, the TLS noise also increases with increasing resonance frequency over the readout band of each tile.

The IDCs couple to incident radiation, and to prevent this radiation from being absorbed in the aluminum section of the MKID a stepped impedance filter has been incorporated in the niobium section of the MKID CPW. This filter reduces the IDC-coupled optical load to a negligible amount.[19] In addition, the aluminum section of the MKID also directly couples to incident radiation,[26] and to minimize this direct absorption the aluminum section was made as small as possible while still retaining a high absorption efficiency to the power coupled via the microstrip from the antenna. To further reduce the amount of optical power directly absorbed by the aluminum section, a polarizing grid was installed in the optical path in late 2012 (the direct absorption is sensitive to both polarizations, while the antennas are only sensitive to a single polarization direction). The optical efficiency of the antennas was unchanged after installation of the polarizing grid, but the grid did reduce the directly absorbed power by a factor of $\simeq 1.6$. This is less than the ideal factor of 2, but still represents a significant improvement. With the grid in place, the direct absorption optical efficiency is $\lesssim 10\%$ relative to the main beam efficiency, and approximately 25% of the direct absorption is coupled to ambient temperature surfaces with the remaining 75% coupling to the atmosphere. As a result, the effective optical load from the direct absorption is $\simeq 5$ K.

The geometry of the lumped-element band-defining filters was refined based on engineering-grade focal plane tiles produced during the instrument development phase, and the measured bandpasses from those tiles agreed well with the designed values.[19] Measurements of the science-grade focal plane tiles were made in early 2013, and those bandpasses show a downward shift in frequency of $\simeq 3\%$ relative to the earlier devices (see Figure 2). This

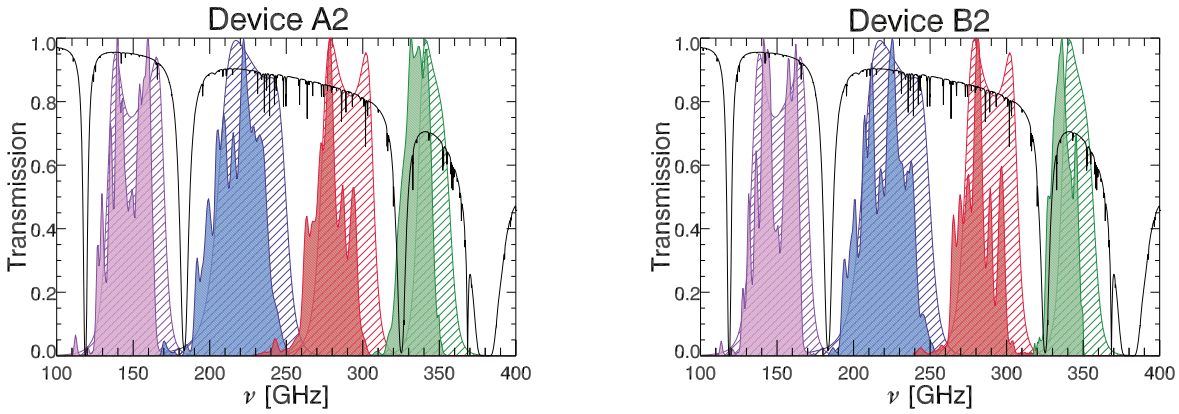

Figure 2. MUSIC bandpasses. The solid-filled regions show the measured bandpasses and the hashed-filled regions show the designed bandpasses. The measured bandpasses are shifted by $\simeq 3\%$ to lower frequency due to an increase in ε of the Si_3N_4 dielectric relative to the engineering-grade tiles used to calibrate the filter geometry. Overlaid in black on each plot is the atmospheric transmission spectrum from the CSO for 2.0 mm of precipitable water vapor (the median at the CSO is 1.68 mm), showing that the 350 GHz band overlaps with the atmospheric absorption feature at 325 GHz. The left plot shows bandpasses from the tile labeled A2 and the right plot shows bandpasses from the tile labeled B2. In each case, the measured bandpasses have been averaged over approximately half of the detectors on the tile, which corresponds to approximately 20 detectors in each observing band.

shift was caused by an increase in the ratio of the dielectric constant ε to the thickness d of the Si_3N_4 dielectric used for the science-grade tiles, with direct measurements of capacitive test devices on the tiles showing an increase of 6% in ε/d between the final engineering-grade tiles and the science-grade tiles. Due to the locations of the observing bands relative to optically-thick absorption features in the atmosphere, this bandpass shift has little impact on the 150, 230, and 290 GHz observing bands, but it has a significant impact on the 350 GHz band (which shifted far enough to significantly overlap with a water absorption line at $\simeq 325$ GHz). As a result, the sensitivity of the 350 GHz observing band is noticeably degraded.

The science-grade tiles for MUSIC were fabricated in 2012, and the yield from this fabrication run was lower than expected. The first sets of tiles suffered from discontinuities in the feedlines, but these discontinuities were largely eliminated in later tiles due to improvements in the cleaning process between fabrication steps. In total, seven of the science-grade tiles have feedline continuity, and all of these tiles also have a high resonator yield. Two of these tiles, labeled "A2" and "B2", perform well, with MKID yields as described below. For each tile, approximately 95% of the fabricated MKIDs are detected via a network analyzer sweep. Of these, approximately 85% are separated by more than 200 kHz from the nearest MKID, which was set as the threshold for collisions between MKIDs*. In addition, a similar number of resonators are discarded due to having highly distorted resonances, low quality factors, and/or atypical behavior with changes in readout power. Furthermore, a comparable number of resonators are also discarded because they have low responsivities and/or higher noise levels compared to the other detectors. The end result is a detector yield of approximately 55% on tiles A2 and B2 (see Table 1). Besides A2 and B2, the other five tiles with good device yields have bandpasses that are significantly shifted from the designed values, with a shift that ranges from 10–20%. As a result, these five tiles have not been extensively used for science observations and the characteristics of these tiles are not presented in this manuscript.

*The MKIDs have resonant frequencies of $\simeq 3.5$ GHz and quality factors of $\simeq 10^5$, resulting in resonance widths of $\simeq 35$ kHz. Therefore, a threshold of 200 kHz ensures resonator separations of at least 5–6 resonance widths.

device	design	MKIDs detected	un-collided	un-distorted/low-Q/power	noise/response	optical
A2	288	277	227	190	166	143
B2	288	272	237	190	159	138

Table 1. MUSIC device yield. From left to right the columns show the designed number of MKIDs for each tile, the number of MKIDs detected via a network analyzer sweep, the number of MKIDs that are at least 200 kHz from the nearest MKID, the number of MKIDs that also show resonances with the expected shapes, quality factors, and power handling, the number of MKIDs that also show the nominal responsivity and noise properties, and the number of MKIDs that are also optically coupled (each tile contains some dark resonators for characterization)..

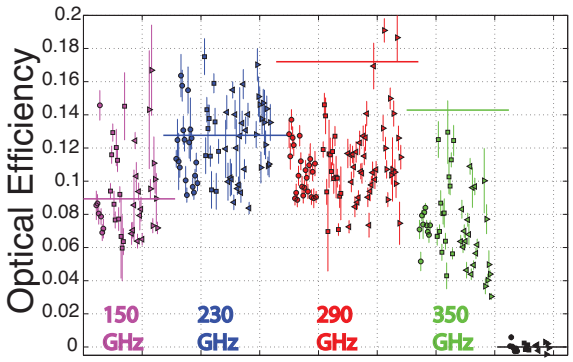

Figure 3. Measured optical efficiency of the MUSIC detectors. Each data point with an error bar represents a single MKID, and the points are color-coded from left to right (purple = 150 GHz, blue = 230 GHz, red = 290 GHz, green = 350 GHz, black = dark detector). The horizontal lines represent the predicted optical efficiency for each band, including losses due to Lyot stop spillover, the efficiency of converting optical power into quasiparticles within the MKID, losses in the optical filters, and radiative and microstrip losses in the antennas. The measured values match the predictions in the 150 and 230 GHz bands, but are lower than expected in the 290 and 350 GHz bands.

2.2 Optical Configuration

MUSIC is coupled to the CSO via an ambient-temperature optics box that contains three mirrors (two flat and one powered), along with a single powered lens that is at 4 K. The two flat mirrors are required to translate the optical path in order to provide a mounting location for MUSIC, and the first flat mirror is located near the Cassegrain focus of the CSO, which has a focal ratio of $\simeq 12.5$. The third mirror has an off-axis ellipsoidal profile, and provides a focal ratio of $\simeq 16$, along with an image of the CSO primary mirror. A 4 K Lyot stop is placed at the location of the primary image, which defines a circular illumination pattern of diameter 9.0 m on the 10.4 m diameter primary. In the original configuration, the lens provides an average focal ratio of 3.45 over the $14'$ diameter focal plane, along with a focal surface that is approximately flat, telecentric, and has a strehl ratio in the MUSIC bands that is above the diffraction limit. It is constructed from ultra-high molecular weight polyethylene (UHMWPE), coated on both sides with single layers of 250 μm thick Porex PM23J to reduce reflections. The lens is as thin as possible given its diameter and curvature (its thickness is 63.5 mm), and it has a transmission efficiency of 80–90% across the MUSIC observing bands. The antennas used to optically couple the MKIDs are 4.2 mm in size with center-to-center spacings of 5.0 mm, resulting in a detector spacing that corresponds to 0.73–1.66 $(f/\#)\lambda$ for the MUSIC observing bands.

The optical efficiencies of the detectors have been characterized in detail, and are described in Ref. 20. In brief, the measured optical efficiencies of the 150 and 230 GHz observing bands are in good agreement with the predicted values of 9% and 13% (the low optical efficiencies are largely due to the small pixel scale in $(f/\#)\lambda$). In the 290 and 350 GHz bands the measured optical efficiencies are a factor of $\simeq 1.5$ and $\simeq 2.0$ lower than expected, and the cause of these lower optical efficiencies is not fully understood (see Figure 3), but a likely cause is excess loss in the microstrip that was not seen in engineering-grade devices.

In early 2014 the optical system was reconfigured. Specifically, the location and geometry of the of the lens was changed in order to speed up the system to an average focal ratio of 2.19 over the focal plane. This reconfiguration was motivated by the significantly better performance of the A2 and B2 tiles compared to the other science-grade tiles, and provides more efficient optical coupling to those tiles while reducing the total focal plane footprint from eight tiles to two tiles (the angular size covered by the focal plane was also reduced from $14'$/side to $11.5'$/side). The gain in optical coupling with the reconfiguration is possible due to the relatively small pixel scale used in the original design ($\simeq 1(f/\#)\lambda$), which results in a significant loss in optical efficiency due to spillover at the Lyot stop. Optical tests of the updated configuration have not yet been performed, but physical optics simulations in Zemax indicate that the per-detector optical efficiency will increase by up to a

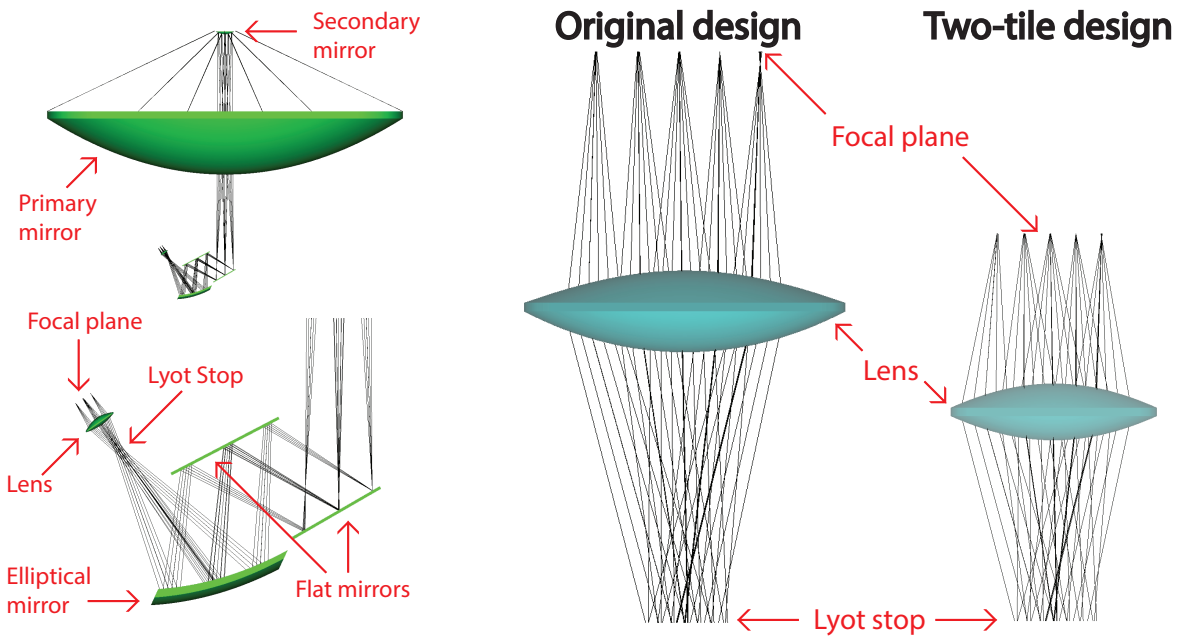

Figure 4. The MUSIC optical system. The upper left image shows the entire system, including the 10.4 m primary mirror of the CSO. The lower left image shows the two folding flat mirrors, the powered elliptical mirror, and powered lens, with the focal plane in the upper left. The middle image shows a further zoomed in view of the optical system from the Lyot stop to the focal plane based on the original design described in Ref. 18 (note that it has been rotated 35 degrees clockwise compared to the left hand images). The right image shows the updated lens design for a two-tile configuration, and it is scaled to match the middle image. The new design is faster than the original design, with a final focal ratio of 2.19 compared to 3.45, and provides more efficient optical coupling to the reduced two-tile focal plane.

factor of two compared to the original optical design (see Table 2). As described in detail in Ref. 20, MUSIC's sensitivity is limited by TLS noise, and therefore the sensitivity is expected to improve as the square root of the optical efficiency.[†] In addition, there will be a slight reduction in the optical load on the detectors because less power will couple to the inside of the Lyot stop. However, the new optical configuration also results in slightly larger PSFs, particularly in the higher frequency MUSIC observing bands, and point-source sensitivity scales with the solid angle of the PSF. Quantitative estimates of the expected changes in the sensitivity are give in Section 3.4.

As noted in Ref. 19, the original optical design for MUSIC suffered from significant optical coupling to large angles outside the instrument. Measurements made via skydips at the CSO in mid 2012 show spillover fractions of 15%, 12%, 12%, and 17% at 150, 230, 290, and 350 GHz.[‡] Approximately all of this large-angle coupling is to ambient temperature surfaces, and so the resulting optical load is significant. The cause of the large-angle coupling is thought to be scattering within the optical system; a time-reverse scattering off of the inside surface of the Lyot stop can then scatter off of the focal plane surface and directly exit the instrument at wide angles. The relatively small pixel scale of the original MUSIC configuration results in significant coupling between the antennas and these inside surfaces of the Lyot stop. For example, in the 150 GHz band the coupling fraction to the Lyot stop surfaces is approximately 300% relative to the main beam, and therefore the Lyot stop surfaces

[†]The frequency RMS due to the TLS noise is constant, the power coupled to the MKID is proportional to the optical efficiency, and the frequency responsivity of the MKID is inversely proportional to the square root of the optical loading. As a result, in the TLS-noise-limited case, the MKID sensitivity improves as the square root of the optical efficiency.

[‡]These values are slightly different compared to the spillover values given in Ref. 19, which were based on lab measurements of an engineering-grade device.

Configuration	150 GHz		230 GHz		290 GHz		350 GHz	
	Lyot eff.	FWHM	Lyot eff.	FWHM	Lyot eff.	FWHM	Lyot eff.	FWHM
Original	0.28	$44''$	0.51	$31''$	0.67	$25''$	0.76	$22''$
Two-tile	0.56	$44''$	0.79	$32''$	0.84	$28''$	0.85	$25''$

Table 2. Calculated performance of the original eight-tile and the reconfigured two-tile optical designs. From left to right the columns show the four MUSIC observing bands, and within each band the optical efficiency through the Lyot stop, along with the FWHM of the PSF, is given. Note that the efficiency and FWHM numbers are based on calculations using Zemax for a pixel at the center of the focal plane. The top row shows the original optical design which illuminates eight detector tiles covering a $14'$ field of view (FOV), and the bottom row shows the reconfigured design which illuminates two detector tiles with an $11.5'$ FOV. Due to the fact that MUSIC is TLS-noise-limited, the per detector sensitivity will improve proportional to the square root of the Lyot stop optical efficiency. Surface brightness sensitivity is independent of FWHM, but point-source sensitivity scales with FWHM squared.

Configuration	150 GHz	230 GHz	290 GHz	350 GHz
Original (measured)	85 K	70 K	80 K	165 K
Two-tile (predicted)	77 K	64 K	75 K	160 K
Two-tile w/ baffle (predicted)	32 K	44 K	55 K	120 K

Table 3. MUSIC optical load. The first row gives the measured optical load for the original eight-tile configuration, and these values are described in detail in Ref. 20. The second row gives the expected load after the optical reconfiguration to speed up the system and illuminate two tiles instead of eight, with the reduction in load due to the lower coupling between the detectors and the inside of the Lyot stop. The third column provides the expected load with the new baffling installed, assuming that the baffling eliminates the large-angle coupling. This value is estimated from the skydip measurements presented in Ref. 20, assuming that 10 K of the spillover load is due to the telescope itself and will not be eliminated by the new baffling.

only need to be $\simeq 5\%$ reflective to explain the measured large-angle coupling.

To reduce the reflectivity of the Lyot stop surfaces, they have been covered with carbon and stainless-steel loaded Stycast.[27] Although the thermal properties of this coating make it well-suited to cryogenic applications, it does have a reflectivity of $\simeq 10\%$ at submillimeter wavelengths,[28,29] which is enough to explain the large angle coupling seen by MUSIC. Therefore, in order to mitigate this coupling a set of cylindrical baffles was installed on the inside of the Lyot stop in late 2012. This baffling scheme is not ideal given the geometry of the scattering, but was the best option that did not involve a major fabrication effort. Compared to the previously measured results, skydip measurements from the CSO in 2013 indicate that this baffling slightly reduced the large-angle spillover fraction to values of 14%, 10%, 9%, and 18% at 150, 230, 290 GHz, and 350 GHz,[§] but the optical loading from this coupling is still significant. Therefore, as part of the reconfiguration to the new lens, a new set of baffles was also installed in the system. These baffles have conical cross sections, and the inside of the Lyot stop also has a conical profile to prevent scattering back towards the focal plane surface (see Figure 6). It is expected that this new baffling will reduce the large-angle coupling to a negligible amount (see Table 3). In the TLS-noise-dominated limit, the sensitivity should improve as the square root of the optical load[¶], and quantitative estimates for this improvement are given in Section 3.4.

2.3 Cryomechanical System

The MUSIC cryomechanical design is described in detail in Refs. 16,19. The measured performance of the system agrees well with expectations, and a brief summary of the system is given below. A Cryomech PT-415 is used to provide the first two cold stages, and the first stage typically runs at $\simeq 60$ K. The temperature of the second stage depends on the number of cryogenic amplifiers that are powered on, and with two amplifiers powered on in order to readout tiles A2 and B2 the stage runs at $\simeq 3.5$ K. To minimize the vibrations transferred from the PT-415 to the cryostat, the remote motor is bolted to the telescope support structure away from the cryostat, flexible copper

[§]The 350 GHz spillover is slightly higher than the previous measurements, although in both cases there is significant scatter in the results for that observing band.

[¶]The detector responsivity scales as the inverse of the square root of the optical load and the frequency RMS of the TLS noise is constant.

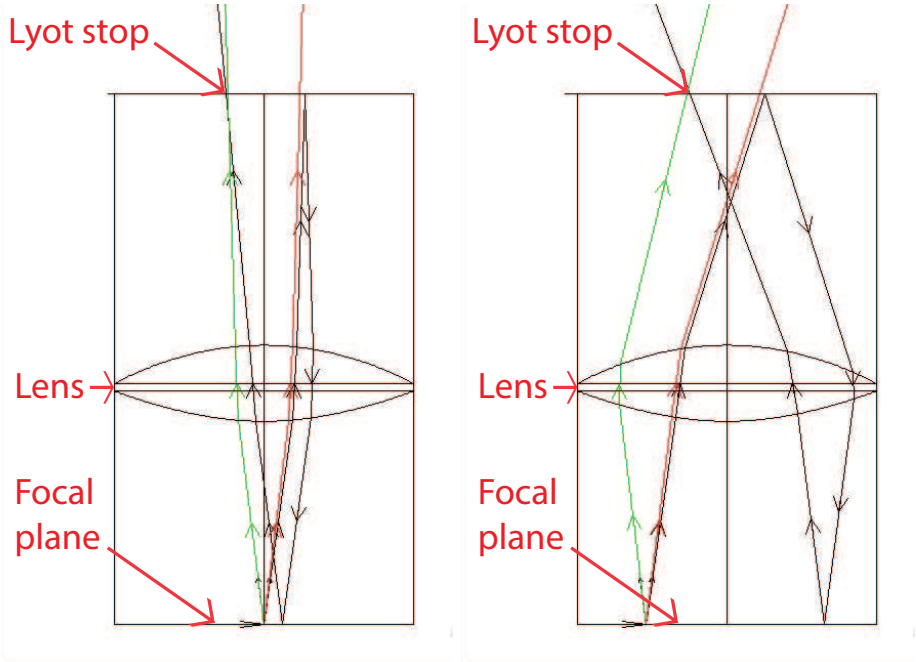

Figure 5. Time-reverse ray tracing from an antenna on the focal plane with the original optical design. The left image shows an antenna near the center of the focal plane, and the right image shows an antenna towards the edge of the focal plane. The red and green rays represent the extreme opening angles that will pass through the Lyot stop and therefore propagate through the rest of the optical system. The black ray is at a slightly larger angle, and is scattered back by the inside surface of the Lyot stop. It can then scatter off of the focal plane surface and exit the instrument at a large angle relative to the nominal optical path for the given antenna.

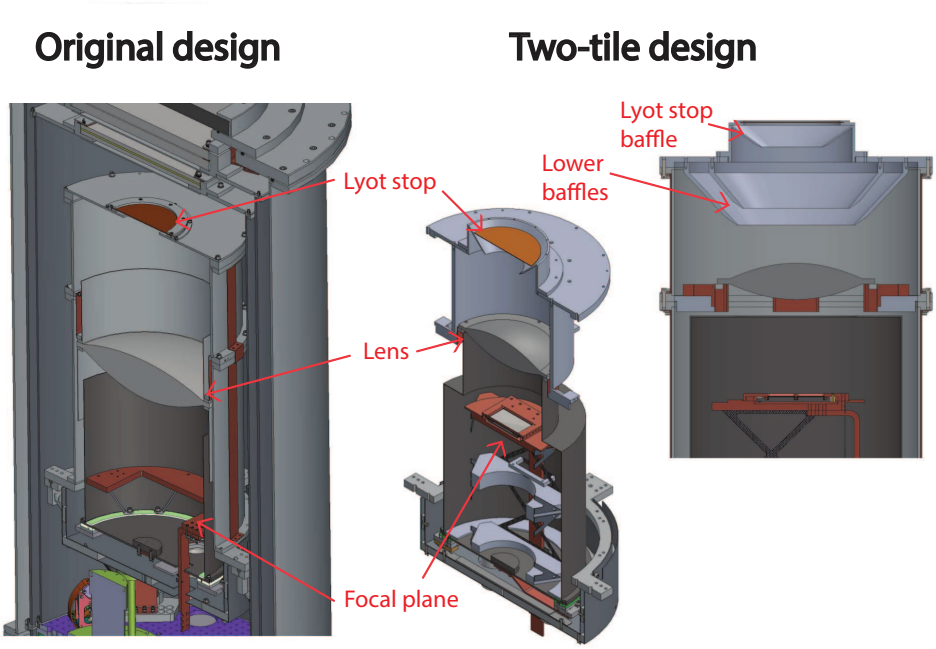

Figure 6. MUSIC internal optical hardware. The left image shows an isometric cut of the full cryostat based on the original eight-tile design, with the ambient temperature shield on the outside. Time-reverse scattering off of the flat surfaces around the Lyot stop can then scatter off of the focal plane and outside the cryostat at large angles (see Figure 5). The middle image shows the reconfigured two-tile optical system with a scale approximately matching the left image. Note the shorter optical path, and higher locations of the lens and focal plane relative to the Lyot stop. The right image shows the full set of baffles that have been installed as part of the new optical configuration in order to reduce the optical coupling to large angles via scattering off of the surfaces around the Lyot stop.

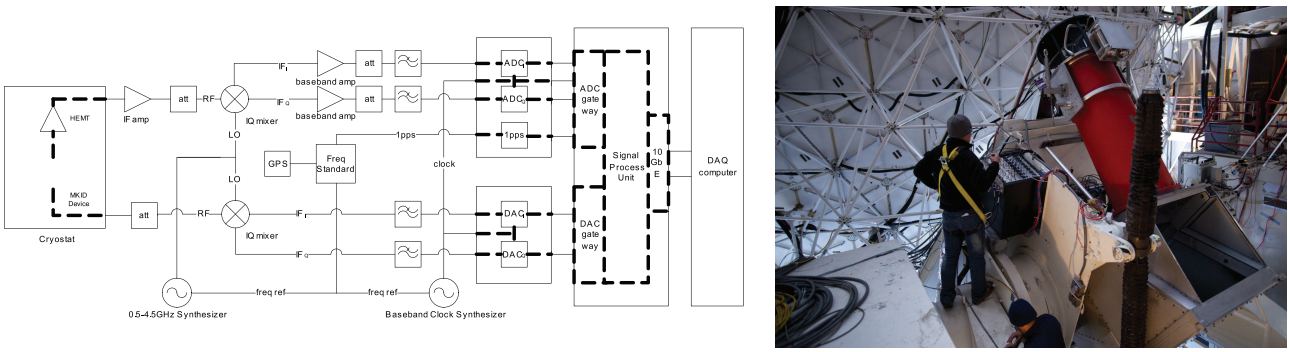

Figure 7. MUSIC readout electronics. The schematic on the left provides an overview of the entire system. The photo on the right shows the red MUSIC cryostat installed at the CSO with Ran Duan working on one of the black electronics crates. The crate contains eight pairs of readout boards, which is enough for four focal plane tiles (a second crate, not shown in the photo, is mounted beside the first crate in order to read out all eight tiles).

straps are used to thermally connect the PT-415 cold heads to the associated cold stages in the cryostat, and the PT-415 assembly is attached to the cryostat via a stainless steel bellows. Given the superconducting transition temperature of aluminum (1.2 K), along with the expected optical load on the detectors, the MKIDs need to be operated at $\simeq 300$ mK in order for the number of thermally produced quasiparticles to be negligible compared to the number of optically produced quasiparticles. A Chase cryogenics closed-cycle three-stage 3He/3He/4He sorption refrigerator is used to produce the low temperature stage for the focal plane, which runs at $\simeq 240$ mK. The refrigerator is cycled via an automated routine which requires $\simeq 6$ hours to run, and the hold time is in excess of 24 hours. Due to the diurnal observing schedule at the CSO, the refrigerator is cycled once per day during the daylight hours.

2.4 Readout System

The MUSIC readout electronics are described in detail in Refs. 15,19, and a brief summary is provided below (see Figure 7). The heart of the readout system is based on CASPER Reconfigurable Open Architecture Computer Hardware (ROACH) boards coupled to custom-built DAC/ADC boards, with two pairs of boards for each focal plane tile. Each ROACH FPGA provides a playback buffer to the DAC at $\simeq 500$ MHz that is 2^{16} samples in length and contains a comb of 192 probe frequencies, or 384 probe frequencies per focal plane tile. One probe is centered on the resonance frequency of each MKID, and the remaining 96 are spaced throughout the readout band to use as off-resonance diagnostics. Given the buffer length and sample rate, the probe frequencies can be specified to 7.5 kHz. The output of the DAC is then upconverted via an IQ mixer to the resonator band at 3–4 GHz, and subsequently passes through a variable attenuator. The attenuator allows the power level of the probe signals to be varied without changing the power level at either the DAC output or the IQ mixer input. The probe signals from the two pairs of readout boards for each focal plane tile are then combined and routed into the cryostat on a single coaxial cable. To reduce the thermal noise transmitted by this coaxial cable to a negligible amount, there is 20 dB of attenuation at the second PT-415 stage and an additional 10 dB of attenuation at the intermediate stage of the 3He/3He/4He refrigerator.

The probe signal is then sent through the feedline on the focal plane tile and input to a cryogenic HEMT amplifier mounted to the second PT-415 stage. The HEMTs were provided by S. Weinreb, and have measured noise temperatures of 3–5 K over the 3–4 GHz band relevant for MUSIC. The gain of the HEMTSs is approximately 30 dB. After exiting the cryostat, the signal is split in order to be routed to the two pairs of boards used for each focal plane tile, and then further amplified. The signals are mixed back down to baseband via the IQ mixer, after passing through a variable attenuator that is used to ensure the proper power level at the IQ mixer's input. Next, the signals are digitized by the ADCs after passing through anti-aliasing filters that reduce the usable bandwidth to $\simeq 450$ MHz. The same FPGA that provides the playback buffer then performs a 2^{16}-sample FFT and selects the FFT bins that correspond to the 192 probe frequencies in the buffer. These complex-valued outputs are then downsampled from 7.5 kHz to 100 Hz and merged with the 100 Hz pointing information provided by the CSO.

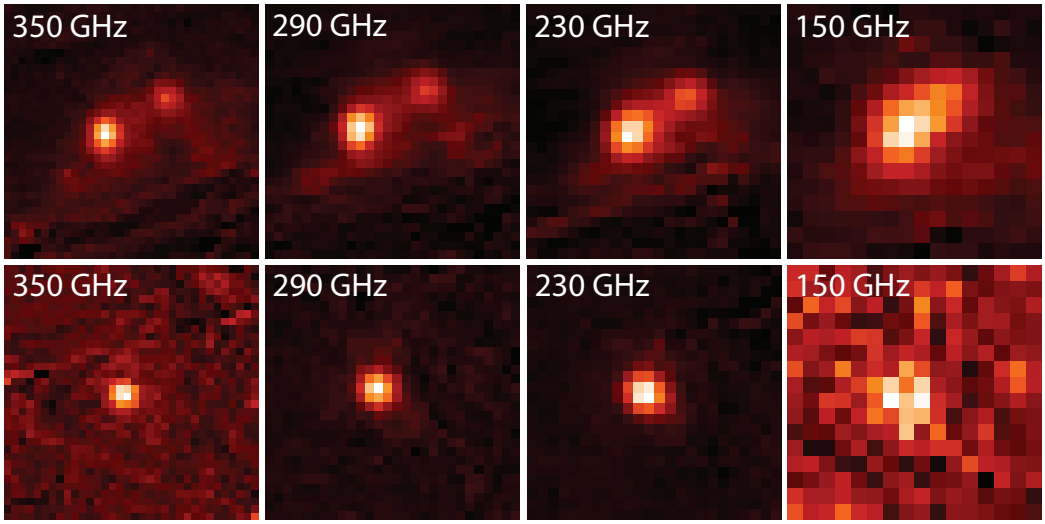

Figure 8. MUSIC four-band images of W51 (top) and a Bolocam Galactic Plane Survey (BGPS[31]) source at 010.47+00.03 (bottom). All of the thumbnails are $4' \times 4'$ in size.

3. ON-SKY PERFORMANCE

MUSIC was installed at the CSO in April 2012, and three short engineering runs were conducted in 2012. In September 2013 a longer science run, lasting approximately six weeks, was performed. An overview of these observing runs, along with the associated data calibrations, reductions, and measured sensitivities is provided below.

3.1 Observing Programs

As detailed in Section 1, MUSIC is well suited to observations of dusty star-forming galaxies, the SZ signal from massive clusters, and cold prestellar cores. For the initial science run in 2013, the observing time was split approximately evenly between these three types of science targets. Specifically, a total of 34 cold cores were observed for a combined on-source time of approximately 45 hours. Three dusty star-forming galaxies, selected from the SPIRE-HeRS survey to be bright and red in the three SPIRE bands, were observed for a total of just over 40 hours on-source. Finally, the massive cluster MACS J2211.7, selected as one of the SZ brightest objects from the Bolocam X-ray/SZ sample[30] with an RA that is observable in September, was observed for a total of nearly 70 hours on-source. Almost all of the observations were made using Lissajous scans with an RMS scan speed of $\simeq 240''$/sec and an amplitude of $90''$ with the source centered on the inner half of the A2 tile, although some of the cold core observations were performed using larger raster scans, with map sizes up to $90' \times 90'$.

As described below, the reduction of these data is ongoing, although scientifically interesting results from all three science programs are expected. Initial maps of the cold cores show that nearly all are detected at high significance in the 230 and 290 GHz observing bands. In addition, many are detected in either or both of the 150 and 350 GHz observing bands (see Figure 8). These measurements will help discriminate between the amount of dust and free-free emission from these cores. Jackknife coadds of the SPIRE-HeRS-selected dusty galaxies indicate that the RMS/beam is approximately 4, 2.5, and 4 mJy at 150, 230, and 290 GHz (the 350 GHz data are significantly noisier due to the overlap of its bandpass with an atmospheric absorption line). Based on extrapolations from the three-band SPIRE measurements, these sources should be detected at high significance in the 230 and 290 GHz observing bands. Similar jackknife coadds of the MACS J2211.7 observations indicate noise RMSs a factor of $\simeq 2$ lower, which, based on the Bolocam measurements, should result in a high significance resolved detection at 150 GHz and a moderate significance detection at 290 GHz. The null of the thermal SZ signal is near 230 GHz, and those data will be used to search for a possible kinetic SZ signal.

3.2 Calibration

The MUSIC data requires three basic types of calibration: pointing reconstruction, PSF characterization, and flux calibration. In general, all of these calibrations are determined using frequent observations of bright unresolved sources with known brightnesses. In particular for MUSIC, Mars, Uranus, Neptune, and G34.3 have been used. The MUSIC pointing reconstruction and PSF characterization is described in detail in Ref. 19, and those results are briefly summarized below.

In order to fully reconstruct the MUSIC pointing, the offset between the location of each pixel relative to the coordinates recorded by the telescope needs to be determined. The MUSIC optics were designed to be sufficiently stiff such that any motion due to accelerations would produce a negligible pointing shift at the focal plane (equivalent to $\lesssim 1''$), and therefore a single set of offset values should be valid for any position on the sky (this was not the case for MUSIC's predecessor, Bolocam, which had global shifts of $20''$–$30''$ over the sky[32]). During the first MUSIC engineering run, pointing offsets were determined based on observations of Mars over its full track above 25 degrees elevation, and the RMS of these offsets is $\simeq 3''$. Subsequent measurements using Uranus and G34.3 have produced similar RMS values. These RMSs are comparable to the RMS pointing achieved with SHARC II,[33] and are thought to be limited by the CSO itself. These measurements confirm that the stiffness of the MUSIC optics matches the design goal, and therefore a single pointing offset for each pixel is used for all of the data.

To date, the main beams of the MUSIC PSFs have been accurately measured, mainly from observations of Mars. A small correction is applied to these measurements to account for the finite angular size of Mars. The median measured FWHMs of the PSFs are $23''$, $26''$, $31''$, and $44''$ at 350, 290, 230, and 150 GHz, with RMS variations of $\lesssim 5\%$ over the focal plane. These numbers are in reasonably good agreement with predictions from Zemax physical optics calculations, although the measured PSFs in the two high frequency bands are approximately 5% larger than predicted. The sidelobe response of the PSFs has not yet been characterized in detail. However, initial measurements limited by noise indicate that any sidelobe response must be below -20, -25, -25, and -20 dB relative to the peak of the main beam at 350, 290, 230, and 150 GHz.

The flux calibration procedure for MUSIC is based on the general algorithm developed for Bolocam.[32] In brief, the DC resistance of the Bolocam bolometers is a monotonic function of the total optical loading, which is directly related to the in-band atmospheric attenuation of the signal. In addition, the responsivity of the bolometers is also a monotonic function of the DC bolometer resistance. As a result, the Bolocam flux calibration is determined by fitting a parametric model to the focal-plane-averaged DC bolometer resistance versus the calibration factor in units of nV/Jy. Because the atmospheric attenuation is directly accounted for in this fit, the calibration factors are referenced to the intrinsic flux density of the calibrator (i.e., above the atmosphere). For MUSIC, the focal-plane-averaged frequency shift of the MKID resonances, relative to a fiducial measurement of the resonance frequencies, is used in place of the DC bolometer resistance, as it behaves in a completely analogous way (i.e., there is a monotonic relation between the frequency shift and both the total optical loading and the MKID responsivity). The frequency shift is determined using sweeps, which are performed approximately 1–2 times per hour or after moving to a new target. Specifically, data is collected while sweeping the LO frequency of the IQ mixer, which results in a smooth variation of the probe frequencies over the range of interest. First, a broad sweep over a few hundred kHz with steps of 7.5 kHz is performed in order to determine the resonant frequency of each MKID. Next, a shorter sweep of $\simeq 100$ kHz with steps of 2.5 kHz is performed in order to accurately characterize each MKID's complex-valued resonance loop. The frequency shift used for calibration is then determined based on fits to these sweeps.

For all four MUSIC bands, a linear fit of the average frequency shift versus the calibration factor is adequate to describe the data (see Figure 9). The fractional scatter about this fit is 5.0%, 3.2%, 4.4%, and 8.8% at 150, 230, 290, and 350 GHz. Some of this scatter, particularly at 150 and 350 GHz, is likely due to measurement noise rather than fundamental variations in the flux calibration. In addition, the relative calibration between the MKIDs is currently being determined in a sub-optimal way using a subset of Uranus observations. Looking forward, software is now being developed to compute the relative calibration using atmospheric fluctuations (this method was used with Bolocam to obtain $\lesssim 1\%$ relative calibration accuracy), along with accounting for the scatter in the calibration due to measurement noise. Therefore, the scatter values listed above should be considered as upper limits on the accuracy of the MUSIC flux calibration. However, if the above scatter values

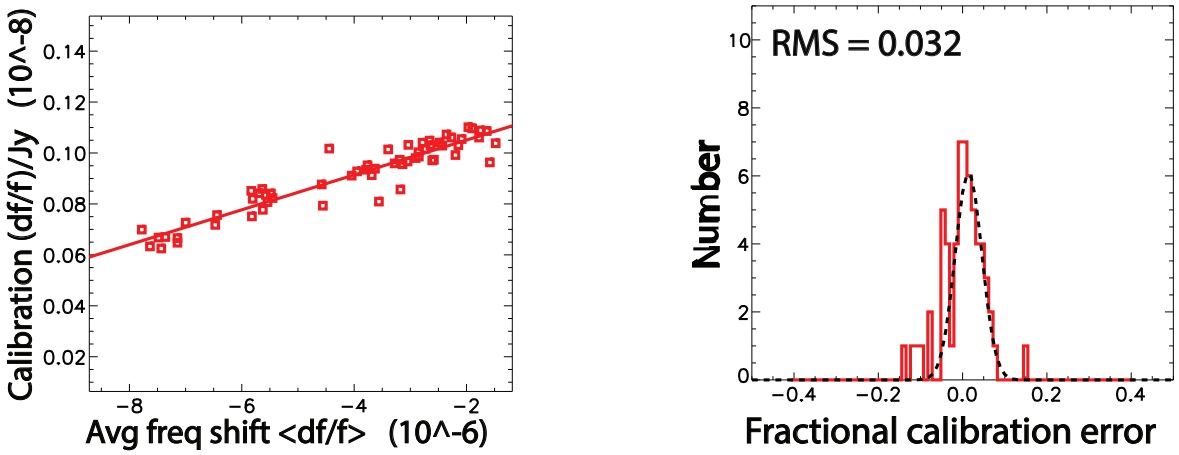

Figure 9. MUSIC flux calibration for the 230 GHz band. Left shows the calibration factor in fractional frequency shift per Jy as a function of the average frequency shift obtained from the sweep performed prior to each observation. There is a monotonic relationship between frequency shift and both detector responsivity and atmospheric opacity, and therefore the average frequency shift is an excellent proxy for the calibration factor. Note that each data point is a single observation of Uranus, and the observations span the entire six-week-long observing run in September 2013. Right shows the fractional deviation of each observation from the linear model fit, and the RMS of this distribution is 3.2%

are combined with the $\simeq 5\%$ uncertainty on the planetary brightness models in the MUSIC observing bands,[34] then the resulting overall flux calibration uncertainty is 7%, 6%, 7%, and 10% at 150, 230, 290, and 350 GHz. These values are comparable to the best results obtained from similar facilities at similar wavelengths (e.g., Refs. 34, 35).

3.3 Data Reduction

The MUSIC data reduction is performed using the Bolocam reduction pipeline as a basis, with MUSIC-specific reduction modules called in place of the modules used for Bolocam. A general description of the modules currently in use is given below, along with plans to expand and improve these modules.

The first step in the data processing is to determine the frequency and dissipation response directions for the complex-valued timestream of each MKID based on resonance fits to the most recent LO sweep performed prior to the given observation. The fractional response of the MKIDs to optical signals is $\simeq 5$–6 times larger in the frequency direction than the dissipation direction. As a result, all of the MUSIC analysis is currently performed using the frequency direction data, although future upgrades will make use of the optimal combination of the frequency and dissipation signals. Next, a search is performed for discrete jumps between consecutive samples in the timestreams, and the entire timestream of any MKID with a jump is flagged and discarded (typically 0–2 timestreams per observation). The cause of these jumps is not known, and the size of the jumps appears to be continuously variable. These jumps will be investigated in more detail in the future. Next, a low pass filter (LPF) is applied to the data at the Nyquist frequency derived from the scan speed and the PSF FWHM, which ranges from $\simeq 8$ Hz for the 150 GHz band to $\simeq 16$ Hz for the 350 GHz band.

At this point, two separate scan-synchronous signals are removed from the timestreams. The first is due to the change in atmospheric opacity as a result of the Lissajous scans, which move the telescope in both azimuth and elevation. The source of the second scan-synchronous signal is not currently understood and is under investigation. This signal is correlated with both the azimuth and elevation motion of the telescope, appears to be constant as a function of the local coordinates of the telescope, and occurs solely in the frequency response direction of the MKIDs with an amplitude that corresponds to a few mJy. The lack of response in the dissipation direction implies that this signal may be magnetic pickup, although pickup due to changes in the Earth's magnetic field as a result of scanning should produce a response that varies with the local coordinates of the telescope. Although the cause of this signal is not well understood, it is well characterized and can be subtracted from the timestreams.

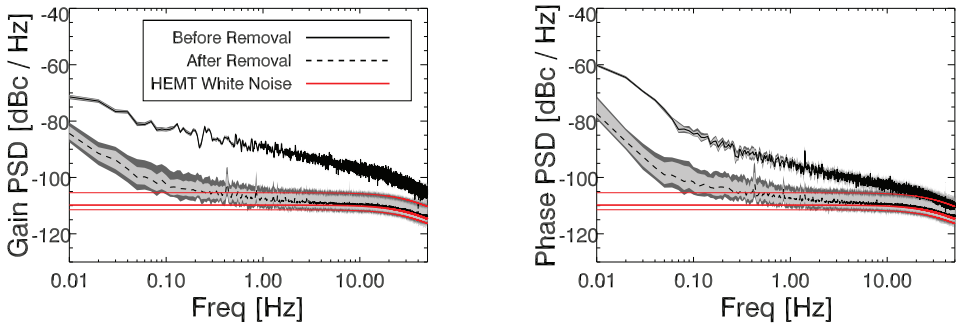

Figure 10. Example noise spectrum measured for the timestreams of the off-resonance probe signals. The left plot shows the gain direction and the right plot shows the phase direction. These are the radial and tangential directions in the complex plane formed by the real and imaginary parts of the Fourier coefficient timestreams recorded by the readout electronics. They are in general not aligned with the frequency and dissipation directions, which are defined relative to each MKID's resonance loop in this plane. The solid black line represents the median raw noise spectrum, and the dashed line represents the median noise spectrum after template subtraction, with 68/95% of the signals falling within the light/dark grey shaded regions. The white noise level of the HEMT amplifier, which varies from probe signal to probe signal based on the readout power, has a median value shown by the thick red line and range between the values given by the thin red lines. The template subtraction recovers this white noise level down to $\simeq 1$ Hz.

The next step is to subtract correlated noise from the electronics and atmospheric fluctuations, which is described in more detail in Ref. 20 (see Figure 10). The correlated electronics noise is due mainly to gain variations in the HEMT amplifier. The off-resonance probe signals are sensitive to these variations, and therefore templates for these variations are formed solely from off-resonance timestreams at readout frequencies close to the MKID readout frequencies. The templates are then correlated and subtracted from each MKID timestream. Because the electronics noise rises steeply at low frequencies in the timestreams, the correlation coefficients are computed in the frequency domain using frequency bins between 10–100 mHz in order to avoid contamination from the detector white noise. The atmospheric fluctuations are approximately common over the entire focal plane, and therefore a template of those fluctuations is formed by taking the average MKID response within each observing band. In the future an algorithm to make use of the full four-band data, particularly the four-band data associated with each individual spatial pixel, will be implemented. For the current reduction, the single-band template is then correlated and subtracted from each MKID timestream, again using data between 10–100 mHz. This full subtraction process is then iterated in order to minimize the impact of atmospheric noise on the electronics template coefficients and vice versa (see Figure 11).

The final step in the data processing is to apply a high-pass filter (HPF) at 0.5 Hz to the timestreams to eliminate the residual atmospheric and electronics noise at low frequency. A noise spectrum is then computed for each MKID timestream, and the data are binned into a map after weighting by the optimally filtered point-source sensitivity of each timestream computed from its noise spectrum and the PSF shape.

3.4 Sensitivity

Based on the data reduction described in Section 3.3, both timestream and map sensitivities have been computed. As a reference point free from residual electronics and atmospheric noise, the timestream sensitivities at 6.5 Hz are in good agreement the instrument noise model, as discussed in detail in Ref. 20. In addition, timestream sensitivities have been computed at 1.0 Hz, where the TLS, residual electronics, and residual atmospheric noise are higher (see Table 4). Note that the signal band, defined by the PSF half-width at half-maximum (HWHM), is from 0 to $\simeq 2.5$–5.0 Hz, and so the band-averaged sensitivity is generally between the 1.0 and 6.5 Hz measurements. Sensitivities have also been computed from the maps, which include noise over the full bandwidth between the Nyquist LPF and the 0.5 Hz HPF, along with degradations due to any correlated noise between detectors. In general, the map-based sensitivities are somewhat worse than expected from the timestream-based sensitivities, likely due to detector correlations from residual atmospheric noise (see Table 4). For reference, the degradation from timestream to map sensitivity is even more severe for MUSIC's predecessor, Bolocam, due to its lower instrument noise levels relative to the atmospheric noise.

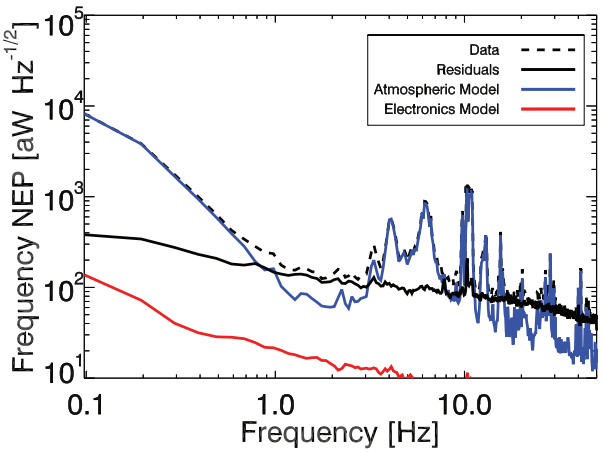

Figure 11. Example noise spectrum for a 230 GHz MKID in the frequency direction. The dashed black line shows the raw data, the blue line shows the template for the atmospheric fluctuations, and the red line shows the template for the electronics noise. After subtracting these templates from the raw data, the resulting noise spectrum is shown as a solid black line. Ref. 20 describes the instrument model for this residual noise in more detail. At 6.5 Hz, the measured noise is well matched by the noises expected from the model, with the dominant contributor being TLS noise. The noise features above $\simeq 3$ Hz that are largely correlated with the atmospheric template are caused by the Lissajous scans. These noise spectra do not include the Nyquist LPF and 0.5 Hz HPF that are applied to the data as part of the data reduction described in Section 3.3.

	MUSIC				Bolocam	
band	150 GHz	230 GHz	290 GHz	350 GHz	140 GHz	270 GHz
timestream values (mJy$\sqrt{\text{sec}}$)						
predicted (6.5 Hz)	180	90	170	530	-	-
measured (6.5 Hz)	280	100	180	510	80	40
measured (1.0 Hz)	560	170	330	910	110	60
map values (mJy$\sqrt{\text{sec}}$)						
measured	360	180	290	930	190	100
improvement factors due to upgrades						
faster optics $\rightarrow$ increased η	0.71	0.80	0.89	0.95	-	-
faster optics $\rightarrow$ larger PSF	1.00	1.07	1.25	1.29	-	-
faster optics $\rightarrow$ lower T_{load}	0.95	0.95	0.97	0.99	-	-
improved baffling	0.64	0.83	0.86	0.87	-	-
predicted after upgrades (mJy$\sqrt{\text{sec}}$)						
total	150	120	270	980	-	-

Table 4. MUSIC sensitivity. The top row shows the predicted timestream sensitivities at 6.5 Hz based on the instrument model described in Ref. 20. The second and third rows show the measured sensitivities at 6.5 Hz and 1.0 Hz for the lower half-band of tile A2 (the coverage in the Lissajous maps used to derive the map based sensitivities is dominated by detectors in this half band). The sensitivities degrade at 1.0 Hz compared to 6.5 Hz due to a combination of TLS noise, residual atmospheric noise, and residual electronics noise. The fourth row shows the measured map sensitivities. For reference, the measured sensitivities of MUSIC's predecessor, Bolocam, are given in the right-hand columns. The significant degradation between timestream sensitivity and map sensitivity for Bolocam is due to detector correlations from residual atmospheric noise. This degradation is much less significant for MUSIC due to its higher noise levels. The fifth through eighth columns provide estimates for the change in point source sensitivity as a result of the recent instrument upgrades described in Section 2.2, which include speeding up the optics and improving the baffling. These factors are computed under the assumption that the sensitivity values are TLS noise limited, which is in general true for the MUSIC detectors. The final row provides the estimated map sensitivities with the upgrades. The 150/230 GHz MUSIC sensitivities should be comparable to the 140/270 GHz Bolocam sensitivities. Note that the 290 and 350 GHz sensitivities suffer from lower than designed optical efficiencies, and the 350 GHz sensitivity is significantly degraded by the overlap of its bandpass with an atmospheric water line.

In Section 2.2 two significant upgrades to MUSIC were described: the focal ratio of the optical system has been sped up to improve the optical efficiency per detector and new baffling has been installed to reduce the optical loading. In addition to increasing the optical efficiency of the system, this change to the focal ratio is also expected to reduce the effective optical load seen by the detectors due to the reduced coupling between the detectors and the surfaces inside the Lyot stop. However, the change also results in slightly larger PSFs, which will degrade MUSIC's point-source sensitivity. The expected change in sensitivity due to these upgrades is quantified in Table 4, under the assumption that the MUSIC detectors are TLS-noise limited, which is in general valid. The overall result is that the 150 and 230 GHz observing bands are expected to achieve per-detector sensitivities that are comparable to MUSIC's predecessor, Bolocam. The sensitivity of the 290 and 350 GHz bands will still be degraded as a result of the low optical efficiency described in Section 2.2, and the 350 GHz sensitivity is further degraded due to the overlap of its bandpass with the atmospheric absorption line at 325 GHz.

4. SUMMARY AND FUTURE PLANS

As described in detail in Ref. 20, the performance of MUSIC is now largely understood, and the predictions of the instrument model are generally in excellent agreement with measurements. The only significant disagreement between the model and the measurements is the low optical efficiency of the 290 and 350 GHz observing bands, which is under investigation and may be caused by losses in the microstrip. Once this discrepancy is understood, then resources to produce new focal plane tiles will be pursued in order to fully populate MUSIC. Any new tiles will also utilize constant-sized IDCs, and the MKID resonant frequencies will be adjusted via the inductive portion of the MKID. This change will significantly reduce the level of TLS noise in the MKIDs towards the high-frequency end of the readout band.

Analysis of the science data collected in September 2013 is proceeding rapidly, and publications with initial results are expected within the next few months. The camera upgrades described in Section 2.2 have recently been completed, and MUSIC is now reinstalled at the CSO. Tests of the new system are underway, and an engineering run is scheduled for late July 2014. If the system performs as expected, then an extended science run will follow later in 2014, with science targets similar to those observed during the September 2013 observing run. The significant improvement in sensitivity expected for the 150 and 230 GHz observing bands should allow for a large increase in the overall science program compared to the September 2013 observing run.

MUSIC will continue to operate from the CSO until the facility is decommissioned from Mauna Kea in 2016–2018. Several options are being pursued to replace and expand the MUSIC focal plane and to extend MUSIC's lifetime beyond that date.

ACKNOWLEDGMENTS

MUSIC was designed and constructed with support from NSF/AST-0705157, NSF/AST-1009939, the Gordon and Betty Moore Foundation, and the Caltech Submillimeter Observatory, which has been supported by NSF/AST-0540882 and NSF/AST-0838261. JS and MIH were partially supported by NASA Postdoctoral Program fellowships, and JS was partially supported by a Norris Foundation Postdoctoral fellowship. JAS and NGC were partially supported by NASA Graduate Student Research Program fellowships and SS was partially supported by a NASA Earth and Space Science fellowship. We acknowledge Kathy Deniston and Barbara Wertz for administrative support and the staff and day crew of the CSO for assistance during design, installation, and commissioning.

REFERENCES

[1] Puget, J.-L., Abergel, A., Bernard, J.-P., Boulanger, F., Burton, W. B., Desert, F.-X., and Hartmann, D., "Tentative detection of a cosmic far-infrared background with COBE.," *Astronomy & Astrophysics* **308**, L5 (Apr. 1996).

[2] Fixsen, D. J., Dwek, E., Mather, J. C., Bennett, C. L., and Shafer, R. A., "The Spectrum of the Extragalactic Far-Infrared Background from the COBE FIRAS Observations," *The Astrophysical Journal* **508**, 123–128 (Nov. 1998).

[3] Lagache, G., Puget, J.-L., and Dole, H., "Dusty Infrared Galaxies: Sources of the Cosmic Infrared Background," *Annual Review of Astronomy & Astrophysics* **43**, 727–768 (Sept. 2005).

[4] Bouwens, R. J., Illingworth, G. D., Oesch, P. A., Franx, M., Labbé, I., Trenti, M., van Dokkum, P., Carollo, C. M., González, V., Smit, R., and Magee, D., "UV-continuum Slopes at $z \simeq 4-7$ from the HUDF09+ERS+CANDELS Observations: Discovery of a Well-defined UV Color-Magnitude Relationship for $z \geq 4$ Star-forming Galaxies," *The Astrophysical Journal* **754**, 83 (Aug. 2012).

[5] Vieira, J. D., Marrone, D. P., Chapman, S. C., De Breuck, C., Hezaveh, Y. D., Weiβ, A., Aguirre, J. E., Aird, K. A., Aravena, M., Ashby, M. L. N., Bayliss, M., Benson, B. A., Biggs, A. D., Bleem, L. E., Bock, J. J., Bothwell, M., Bradford, C. M., Brodwin, M., Carlstrom, J. E., Chang, C. L., Crawford, T. M., Crites, A. T., de Haan, T., Dobbs, M. A., Fomalont, E. B., Fassnacht, C. D., George, E. M., Gladders, M. D., Gonzalez, A. H., Greve, T. R., Gullberg, B., Halverson, N. W., High, F. W., Holder, G. P., Holzapfel, W. L., Hoover, S., Hrubes, J. D., Hunter, T. R., Keisler, R., Lee, A. T., Leitch, E. M., Lueker, M., Luong-van, D., Malkan, M., McIntyre, V., McMahon, J. J., Mehl, J., Menten, K. M., Meyer, S. S., Mocanu, L. M., Murphy, E. J., Natoli, T., Padin, S., Plagge, T., Reichardt, C. L., Rest, A., Ruel, J., Ruhl, J. E., Sharon, K., Schaffer, K. K., Shaw, L., Shirokoff, E., Spilker, J. S., Stalder, B., Staniszewski, Z., Stark, A. A., Story, K., Vanderlinde, K., Welikala, N., and Williamson, R., "Dusty starburst galaxies in the early Universe as revealed by gravitational lensing," *Nature* **495**, 344–347 (Mar. 2013).

[6] Enoch, M. L., Glenn, J., Evans, II, N. J., Sargent, A. I., Young, K. E., and Huard, T. L., "Comparing Star Formation on Large Scales in the c2d Legacy Clouds: Bolocam 1.1 mm Dust Continuum Surveys of Serpens, Perseus, and Ophiuchus," *The Astrophysical Journal* **666**, 982–1001 (Sept. 2007).

[7] Morandi, A., Nagai, D., and Cui, W., "Reconstructing three-dimensional parameters of galaxy clusters via multifrequency Sunyaev-Zeldovich observations," *Monthly Notices of the Royal Astronomical Society* **431**, 1240–1251 (May 2013).

[8] Vikhlinin, A., Kravtsov, A., Forman, W., Jones, C., Markevitch, M., Murray, S. S., and Van Speybroeck, L., "Chandra Sample of Nearby Relaxed Galaxy Clusters: Mass, Gas Fraction, and Mass-Temperature Relation," *The Astrophysical Journal* **640**, 691–709 (Apr. 2006).

[9] George, M. R., Fabian, A. C., Sanders, J. S., Young, A. J., and Russell, H. R., "X-ray observations of the galaxy cluster PKS0745-191: to the virial radius, and beyond," *Monthly Notices of the Royal Astronomical Society* **395**, 657–666 (May 2009).

[10] Nagai, D., Lau, E. T., Avestruz, C., Nelson, K., and Rudd, D. H., "Predicting Merger-induced Gas Motions in ΛCDM Galaxy Clusters," *The Astrophysical Journal* **777**, 137 (Nov. 2013).

[11] Oliver, S. J., Bock, J., Altieri, B., Amblard, A., Arumugam, V., Aussel, H., Babbedge, T., Beelen, A., Béthermin, M., Blain, A., Boselli, A., Bridge, C., Brisbin, D., Buat, V., Burgarella, D., Castro-Rodríguez, N., Cava, A., Chanial, P., Cirasuolo, M., Clements, D. L., Conley, A., Conversi, L., Cooray, A., Dowell, C. D., Dubois, E. N., Dwek, E., Dye, S., Eales, S., Elbaz, D., Farrah, D., Feltre, A., Ferrero, P., Fiolet, N., Fox, M., Franceschini, A., Gear, W., Giovannoli, E., Glenn, J., Gong, Y., González Solares, E. A., Griffin, M., Halpern, M., Harwit, M., Hatziminaoglou, E., Heinis, S., Hurley, P., Hwang, H. S., Hyde, A., Ibar, E., Ilbert, O., Isaak, K., Ivison, R. J., Lagache, G., Le Floc'h, E., Levenson, L., Faro, B. L., Lu, N., Madden, S., Maffei, B., Magdis, G., Mainetti, G., Marchetti, L., Marsden, G., Marshall, J., Mortier, A. M. J., Nguyen, H. T., O'Halloran, B., Omont, A., Page, M. J., Panuzzo, P., Papageorgiou, A., Patel, H., Pearson, C. P., Pérez-Fournon, I., Pohlen, M., Rawlings, J. I., Raymond, G., Rigopoulou, D., Riguccini, L., Rizzo, D., Rodighiero, G., Roseboom, I. G., Rowan-Robinson, M., Sánchez Portal, M., Schulz, B., Scott, D., Seymour, N., Shupe, D. L., Smith, A. J., Stevens, J. A., Symeonidis, M., Trichas, M., Tugwell, K. E., Vaccari, M., Valtchanov, I., Vieira, J. D., Viero, M., Vigroux, L., Wang, L., Ward, R., Wardlow, J., Wright, G., Xu, C. K., and Zemcov, M., "The Herschel Multi-tiered Extragalactic Survey: HerMES," *Monthly Notices of the Royal Astronomical Society* **424**, 1614–1635 (Aug. 2012).

[12] Planck Collaboration, Ade, P. A. R., Aghanim, N., Arnaud, M., Ashdown, M., Aumont, J., Baccigalupi, C., Balbi, A., Banday, A. J., Barreiro, R. B., and et al., "Planck early results. XXIII. The first all-sky survey of Galactic cold clumps," *Astronomy & Astrophysics* **536**, A23 (Dec. 2011).

[13] Planck Collaboration, Ade, P. A. R., Aghanim, N., Armitage-Caplan, C., Arnaud, M., Ashdown, M., Atrio-Barandela, F., Aumont, J., Aussel, H., Baccigalupi, C., and et al., "Planck 2013 results. XXIX. Planck catalogue of Sunyaev-Zeldovich sources," *ArXiv e-prints* (Mar. 2013).

[14] Glenn, J., Day, P. K., Ferry, M., Gao, J., Golwala, S. R., Kumar, S., LeDuc, H. G., Maloney, P. R., Mazin, B. A., Nguyen, H., Noroozian, O., Sayers, J., Schlaerth, J., Vaillancourt, J. E., Vayokanis, A., and Zmuidzinas, J., "A microwave kinetic inductance camera for sub/millimeter astrophysics," in [*Society of Photo-Optical Instrumentation Engineers (SPIE) Conference Series*], *Society of Photo-Optical Instrumentation Engineers (SPIE) Conference Series* **7020** (Aug. 2008).

[15] Duan, R., McHugh, S., Serfass, B., Mazin, B. A., Merrill, A., Golwala, S. R., Downes, T. P., Czakon, N. G., Day, P. K., Gao, J., Glenn, J., Hollister, M. I., Leduc, H. G., Maloney, P. R., Noroozian, O., Nguyen, H. T., Sayers, J., Schlaerth, J. A., Siegel, S., Vaillancourt, J. E., Vayonakis, A., Wilson, P. R., and Zmuidzinas, J., "An open-source readout for MKIDs," in [*Society of Photo-Optical Instrumentation Engineers (SPIE) Conference Series*], *Society of Photo-Optical Instrumentation Engineers (SPIE) Conference Series* **7741** (July 2010).

[16] Hollister, M. I., Czakon, N. G., Day, P. K., Downes, T. P., Duan, R., Gao, J., Glenn, J., Golwala, S. R., Leduc, H. G., Maloney, P. R., Mazin, B. A., Nguyen, H. T., Noroozian, O., Sayers, J., Schlaerth, J., Siegel, S., Vaillancourt, J. E., Vayonakis, A., Wilson, P., and Zmuidzinas, J., "The cryomechanical design of MUSIC: a novel imaging instrument for millimeter-wave astrophysics at the Caltech Submillimeter Observatory," in [*Society of Photo-Optical Instrumentation Engineers (SPIE) Conference Series*], *Society of Photo-Optical Instrumentation Engineers (SPIE) Conference Series* **7741** (July 2010).

[17] Maloney, P. R., Czakon, N. G., Day, P. K., Downes, T. P., Duan, R., Gao, J., Glenn, J., Golwala, S. R., Hollister, M. I., Leduc, H. G., Mazin, B. A., McHugh, S. G., Noroozian, O., Nguyen, H. T., Sayers, J., Schlaerth, J. A., Siegel, S., Vaillancourt, J. E., Vayonakis, A., Wilson, P., and Zmuidzinas, J., "MUSIC for sub/millimeter astrophysics," in [*Society of Photo-Optical Instrumentation Engineers (SPIE) Conference Series*], *Society of Photo-Optical Instrumentation Engineers (SPIE) Conference Series* **7741** (July 2010).

[18] Sayers, J., Czakon, N. G., Day, P. K., Downes, T. P., Duan, R. P., Gao, J., Glenn, J., Golwala, S. R., Hollister, M. I., Leduc, H. G., Mazin, B. A., Maloney, P. R., Noroozian, O., Nguyen, H. T., Schlaerth, J. A., Siegel, S., Vaillancourt, J. E., Vayonakis, A., Wilson, P. R., and Zmuidzinas, J., "Optics for MUSIC: a new (sub)millimeter camera for the Caltech Submillimeter Observatory," in [*Society of Photo-Optical Instrumentation Engineers (SPIE) Conference Series*], *Society of Photo-Optical Instrumentation Engineers (SPIE) Conference Series* **7741** (July 2010).

[19] Golwala, S. R., Bockstiegel, C., Brugger, S., Czakon, N. G., Day, P. K., Downes, T. P., Duan, R., Gao, J., Gill, A. K., Glenn, J., Hollister, M. I., LeDuc, H. G., Maloney, P. R., Mazin, B. A., McHugh, S. G., Miller, D., Noroozian, O., Nguyen, H. T., Sayers, J., Schlaerth, J. A., Siegel, S., Vayonakis, A. K., Wilson, P. R., and Zmuidzinas, J., "Status of MUSIC, the MUltiwavelength Sub/millimeter Inductance Camera," in [*Society of Photo-Optical Instrumentation Engineers (SPIE) Conference Series*], *Society of Photo-Optical Instrumentation Engineers (SPIE) Conference Series* **8452** (Sept. 2012).

[20] Siegel, S., Bockstiegel, C., Brugger, S., Czakon, N. G., Day, P. K., Downes, T. P., Duan, R. P., Gao, J., Gill, A. K., Glenn, J., Golwala, S. R., Hollister, M. I., Leduc, H. G., Maloney, P. R., Mazin, B. A., McHugh, S., Miller, D., Noroozian, O., Nguyen, H. T., Sayers, J., Schlaerth, J. A., Vayonakis, A., Wilson, P. R., and Zmuidzinas, J., "Full Instrument Model for the Multiwavelength Sub/millimeter Inductance Camera (MUSIC)," in [*Society of Photo-Optical Instrumentation Engineers (SPIE) Conference Series*], *Society of Photo-Optical Instrumentation Engineers (SPIE) Conference Series* **9153** (July 2014).

[21] Day, P. K., LeDuc, H. G., Mazin, B. A., Vayonakis, A., and Zmuidzinas, J., "A broadband superconducting detector suitable for use in large arrays," *Nature* **425**, 817–821 (Oct. 2003).

[22] Goldin, A., Bock, J. J., Hunt, C., Lange, A. E., Leduc, H., Vayonakis, A., and Zmuidzinas, J., "SAMBA: Superconducting antenna-coupled, multi-frequency, bolometric array," *Low Temperature Detectors* **605**, 251–254 (Feb. 2002).

[23] Goldin, A., Bock, J. J., Hunt, C. L., Lange, A. E., LeDuc, H. G., Vayonakis, A., and Zmuidzinas, J., "Design of broadband filters and antennas for SAMBA," in [*Millimeter and Submillimeter Detectors for Astronomy*], Phillips, T. G. and Zmuidzinas, J., eds., *Society of Photo-Optical Instrumentation Engineers (SPIE) Conference Series* **4855**, 163–171 (Feb. 2003).

[24] Kumar, S., Vayonakis, A., LeDuc, H. G., Day, P. K., Golwala, S., and Zmuidzinas, J., "Mullimeter-Wave Lumped Element Superconducting Bandpass Filters for Multi-Color Imaging," *IEEE Transactions on Applied Superconductivity* **19**, 924–929 (May 2009).

[25] Noroozian, O., Gao, J., Zmuidzinas, J., Leduc, H. G., and Mazin, B. A., "Two-level system noise reduction for Microwave Kinetic Inductance Detectors," in [*American Institute of Physics Conference Series*], Young, B., Cabrera, B., and Miller, A., eds., *American Institute of Physics Conference Series* **1185**, 148–151 (Dec. 2009).

[26] Schlaerth, J., Golwala, S., Zmuidzinas, J., Vayonakis, A., Gao, J., Czakon, N., Day, P., Glenn, J., Hollister, M., Leduc, H., Maloney, P., Mazin, B., Nguyen, H., Sayers, J., and Vaillancourt, J., "Sensitivity Optimization of Millimeter/Submillimeter MKID Camera Pixel Device Design," in [*American Institute of Physics Conference Series*], Young, B., Cabrera, B., and Miller, A., eds., *American Institute of Physics Conference Series* **1185**, 180–183 (Dec. 2009).

[27] Wollack, E. J., Fixsen, D. J., Henry, R., Kogut, A., Limon, M., and Mirel, P., "Electromagnetic and Thermal Properties of a Conductively Loaded Epoxy," *International Journal of Infrared and Millimeter Waves* .

[28] Sharp, E. H., Benford, D. J., Fixsen, D. J., Moseley, S. H., Staguhn, J. G., and Wollack, E. J., "Stray light suppression in the Goddard IRAM 2-Millimeter Observer (GISMO)," in [*Society of Photo-Optical Instrumentation Engineers (SPIE) Conference Series*], *Society of Photo-Optical Instrumentation Engineers (SPIE) Conference Series* **8452** (Sept. 2012).

[29] Wollack, E. J., Kinzer, R. E., and Rinehart, S. A., "A cryogenic infrared calibration target," *Review of Scientific Instruments* **85**, 044707 (Apr. 2014).

[30] Sayers, J., Czakon, N. G., Mantz, A., Golwala, S. R., Ameglio, S., Downes, T. P., Koch, P. M., Lin, K.-Y., Maughan, B. J., Molnar, S. M., Moustakas, L., Mroczkowski, T., Pierpaoli, E., Shitanishi, J. A., Siegel, S., Umetsu, K., and Van der Pyl, N., "Sunyaev-Zel'dovich-measured Pressure Profiles from the Bolocam X-Ray/SZ Galaxy Cluster Sample," *The Astrophysical Journal* **768**, 177 (May 2013).

[31] Ginsburg, A., Glenn, J., Rosolowsky, E., Ellsworth-Bowers, T. P., Battersby, C., Dunham, M., Merello, M., Shirley, Y., Bally, J., Evans, II, N. J., Stringfellow, G., and Aguirre, J., "The Bolocam Galactic Plane Survey. IX. Data Release 2 and Outer Galaxy Extension," *The Astrophysical Journal Supplement* **208**, 14 (Oct. 2013).

[32] Laurent, G. T., Aguirre, J. E., Glenn, J., Ade, P. A. R., Bock, J. J., Edgington, S. F., Goldin, A., Golwala, S. R., Haig, D., Lange, A. E., Maloney, P. R., Mauskopf, P. D., Nguyen, H., Rossinot, P., Sayers, J., and Stover, P., "The Bolocam Lockman Hole Millimeter-Wave Galaxy Survey: Galaxy Candidates and Number Counts," *The Astrophysical Journal* **623**, 742–762 (Apr. 2005).

[33] Kovács, A., Chapman, S. C., Dowell, C. D., Blain, A. W., Ivison, R. J., Smail, I., and Phillips, T. G., "SHARC-2 350 μm Observations of Distant Submillimeter-selected Galaxies," *The Astrophysical Journal* **650**, 592–603 (Oct. 2006).

[34] Sayers, J., Czakon, N. G., and Golwala, S. R., "143 GHz Brightness Measurements of Uranus, Neptune, and Other Secondary Calibrators with Bolocam between 2003 and 2010," *The Astrophysical Journal* **744**, 169 (Jan. 2012).

[35] Dempsey, J. T., Friberg, P., Jenness, T., Tilanus, R. P. J., Thomas, H. S., Holland, W. S., Bintley, D., Berry, D. S., Chapin, E. L., Chrysostomou, A., Davis, G. R., Gibb, A. G., Parsons, H., and Robson, E. I., "SCUBA-2: on-sky calibration using submillimetre standard sources," *Monthly Notices of the Royal Astronomical Society* **430**, 2534–2544 (Apr. 2013).